

Decision Forests vs. Deep Networks: Conceptual Similarities and Empirical Differences at Small Sample Sizes

Haoyin Xu^{1,*}, Kaleab A. Kinfu¹, Will LeVine¹, Sambit Panda¹, Jayanta Dey¹, Michael Ainsworth¹, Yu-Chung Peng¹, Madi Kusmanov¹, Florian Engert², Christopher M. White³, Joshua T. Vogelstein¹, and Carey E. Priebe¹

Abstract. Deep networks and decision forests (such as random forests and gradient boosted trees) are the leading machine learning methods for structured and tabular data, respectively. Many papers have empirically compared large numbers of classifiers on one or two different domains (e.g., on 100 different tabular data settings). However, a careful conceptual and empirical comparison of these two strategies using the most contemporary best practices has yet to be performed. Conceptually, we illustrate that both can be profitably viewed as “partition and vote” schemes. Specifically, the representation space that they both learn is a partitioning of feature space into a union of convex polytopes. For inference, each decides on the basis of votes from the activated nodes. This formulation allows for a unified basic understanding of the relationship between these methods. Empirically, we compare these two strategies on hundreds of tabular data settings, as well as several vision and auditory settings. Our focus is on datasets with at most 10,000 samples, which represent a large fraction of scientific and biomedical datasets. In general, we found forests to excel at tabular and structured data (vision and audition) with small sample sizes, whereas deep nets performed better on structured data with larger sample sizes. This suggests that further gains in both scenarios may be realized via further combining aspects of forests and networks. We will continue revising this technical report in the coming months with updated results.

1 Introduction In the last decade, decision forests (forests hereafter) and deep networks (networks hereafter) have gained prominence in the scientific literature as two of the highest performing techniques for machine learning tasks, including classification. Forests have empirically dominated *tabular* data scenarios, where the relative position of features is irrelevant. More specifically, random forests (RF) and gradient boosted trees (GBDT) have outperformed all other methods in papers comparing various methods on real datasets and machine learning competitions, demonstrating their relevance to the many biomedical applications represented by tabular data [1–5]. In contrast, networks typically dominate other methods on large sample size *structured* data scenarios, where the relative position of features is key for sample identification. Those include vision, audition, text, and autonomous control [6–10].

Nonetheless, the fact that these two approaches dominate in complementary settings have motivated a number of efforts to combine the best of both worlds. For example, Patel et al. [11] pointed out that under certain assumptions, both forests and networks can be cast as max-sum message passing networks, Zhou and Feng [12] combined deep networks with random forests, Shen et al. [13] has worked to make random forests differentiable, and others have made random forests end-to-end trainable [14, 15]. However, the relationship between the internal representations that the two approaches learn has not yet been made explicit, to our knowledge. Here, we illustrate the conceptual commonalities of their representations [16].

The “arbitrarily slow convergence” and the “no free lunch” theorems prove that no one approach can outperform another approach in all problems [17, 18]. While forests and networks are commonly

¹ Johns Hopkins University ² Harvard University ³ Microsoft Research * Corresponding author: hxu36@jhu.edu

The authors acknowledge the National Science Foundation-Simons Foundation’s Research Collaboration on the Mathematical and Scientific Foundations of Deep Learning (MoDL), NSF grant 2031985.

studied to determine their optimal usage, we also compare them empirically to establish guidelines informing the community in which each approach outperforms the other. We do so using tabular, vision, and auditory data, varying training set sample sizes ranging from only a few samples per class up to 10,000 total for each dataset. We limit the sample size because small sample size problems remain a huge challenge in data science, and are essentially ubiquitous in scientific and biomedical datasets.

Viewed conceptually as “partition and vote” schemes, **both forests and networks partition feature space into a union of convex polytopes and predict by voting from the activated nodes**. The similarities provide a unified basic understanding of the relationship between these methods and could be leveraged to explore learning in biological brains. Empirically, forests excel at tabular and structured data (vision and audition) with small sample sizes, whereas networks perform better on structured data with larger sample sizes. This suggests that further gains in both scenarios may be realized via further combining aspects of forests and networks.

2 Conceptual Similarities The classical statistical formulation of the classification problem consists of $(X, Y), (X_1, Y_1), \dots, (X_n, Y_n) \stackrel{iid}{\sim} F_{XY}$, where $\mathcal{T}_n = \{(X_i, Y_i)\}_{i \in \{1, \dots, n\}}$ is the training data and (X, Y) represents the to-be-classified test observation X with true-but-unobserved class label Y . We consider the simplest setting in which X is a feature vector in \mathbb{R}^d and Y is a class label in $\{0, 1\}$. The goal is to learn a classification rule $g_n = g(\cdot; \mathcal{T}_n)$ mapping feature vectors to class labels such that the probability of misclassification $L(g_n) = P[g(X; \mathcal{T}_n) \neq Y | \mathcal{T}_n]$ is small.

Stone’s theorem for universally consistent classification [19, 20] demonstrates, loosely speaking, that a successful classifier can be constructed by first partitioning the input space into cells depending on n , such that the number of training data points in each cell goes to infinity but slowly in n , and then estimating the posterior $\eta(x) = P[Y = 1 | X = x]$ locally by voting based on the training class labels associated with the training feature vectors in cell $C(x) \subset \mathbb{R}^d$ in which the test observation falls. Then, under some technical conditions $L(g_n) \rightarrow L^*$ almost surely for any F_{XY} , where L^* is the Bayes optimal probability of misclassification.

In the context of our formulation of the classification problem, we provide a unified description of the two dominant methods in modern machine learning, forests and networks, as ensemble “partition and vote” schemes. This allows for useful basic insight into their relationship with each other, and potentially with brain functioning.

2.1 Decision Forests Forests, including RF and GBDT, demonstrate state-of-the-art performance in a variety of machine learning settings. Forests have typically been implemented as ensembles of axis-aligned decision trees, but extensions also employ axis-oblique splits [21–23].

Given the training data \mathcal{T}_n , each tree t in a RF constructs a partition $\mathcal{P}_{n,t}$ by successively splitting the input space based on a random subset of data (per tree) and then choosing a hyperplane split (Figure 1) based on a random subset of dimensions (per node) using some criterion for split utility at each node. The depth of each tree is a function of n and involves a tradeoff between leaf purity and regularization to alleviate overfitting. Details aside, each tree results in a partition $\mathcal{P}_{n,t}$ of \mathbb{R}^d and each partition cell—each leaf of each tree—admits a posterior estimate $\hat{\eta}_{n,t,j} = (1/N_{n,t,j}) \sum_{i: X_i \in C_{n,t,j}} I\{Y_i = 1\}$ based on the class labels of the training data feature vectors in cell $C_{n,t,j}$. Under appropriate conditions for partitions $\mathcal{P}_{n,t}$ we have $L(g_n^{RF}) \rightarrow L^*$.

2.2 Deep Networks Networks are extraordinarily popular and successful in modern machine learning [24–27]. Given a network of nodes and edges (Figure 2), each internal node $v_{\ell,k}$ in layer ℓ of the network gathers inputs $\tilde{x}_{\ell-1,j}, j = 1, \dots, n_{\ell-1}$ from the previous layer, weighted by $w_{\ell-1,j,k}, j = 1, \dots, n_{\ell-1}$,

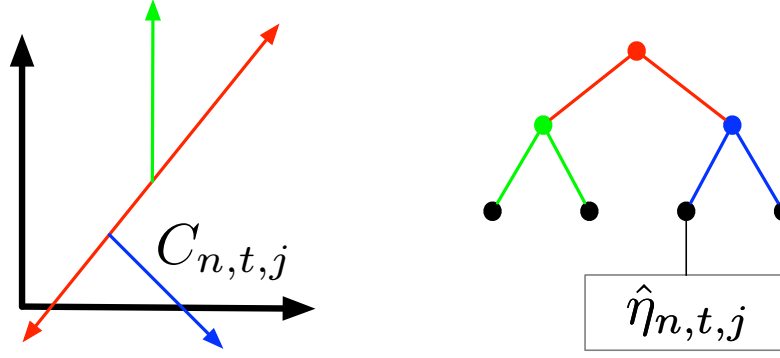


Figure 1: A tree in the forest. Given the random subset $\mathcal{T}_{n,t}$ of the training data allocated to tree t , the root node (red) performs a hyperplane split of \mathbb{R}^d based on a random subset of dimensions; the two daughter nodes (green and blue) split their respective partition cells based on a separate random subset of dimensions allocated to each node; etc. In the end, this tree results in a partition of \mathbb{R}^d with the leaf nodes corresponding to partition cells for which training data class labels yield local posterior estimates. The forest classifies the test observation feature vector X by voting over trees using the cells $C_{n,t}(X)$ in which X falls.

and outputs $\tilde{x}_{\ell,k} = f_{\ell,k}(\sum_j \tilde{x}_{\ell-1,j} w_{\ell-1,j,k}) = f_{\ell,k}(\tilde{X}_{\ell-1}^T W_{\ell-1,k}) = f(\tilde{X}_{\ell-1}^T W_{\ell-1,k} + b_{\ell,k})$. When using the ReLU (rectified linear unit) function $\max(0, \cdot) = (\cdot)^+$ as the activation function f , each node performs a hyperplane split based on a linear combination of its inputs, passing a non-zero value forward if the input is on the preferred side of the hyperplane; data in the cell defined by the collection of polytopes induced by nodes $\{v_{\ell-1,j}\}$, weighted, falls into node $v_{\ell,k}$ and is output based on a partition refinement. Thus, a node in the last internal layer corresponds to a union of hyperplane-induced partition cells, defined via composition of all earlier nodes in the network.

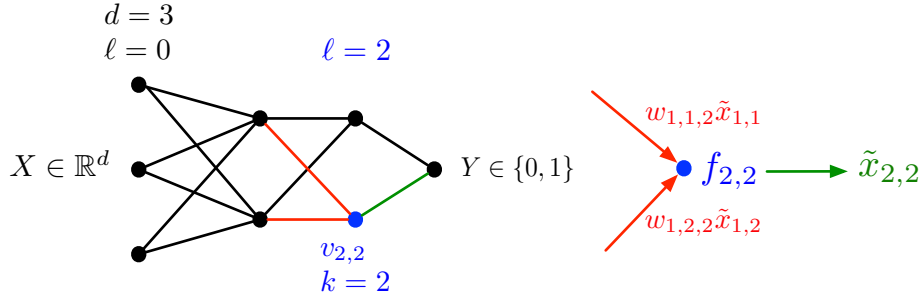


Figure 2: A (shallow) deep network. Given the training data \mathcal{T}_n , the $X_i \in \mathbb{R}^d$ are passed through the network. At layer ℓ and node $v_{\ell,k}$ (the blue node is $v_{2,2}$) the inputs $w_{\ell-1,j,k} \tilde{x}_{\ell-1,j}$ (red) are transformed via hyperplane activation function $f_{\ell,k}$ and output as $\tilde{x}_{\ell,k}$ (green). Thus node $v_{2,2}$ receives non-zero input $w_{1,j,2} \tilde{x}_{1,j} = w_{1,j,2} (X^T W_{0,j} + b_{1,j})^+$ from node $v_{1,j}$ if and only if the linear combination of the multivariate X , $X^T W_{0,j}$, is on the preferred side of hyperplane defined by $f_{1,j}$ (and weight $w_{1,j,2}$ is non-zero). The output of node $v_{2,2}$ is $\tilde{x}_{2,2} = \left(\begin{bmatrix} (X^T W_{0,1} + b_{1,1})^+ \\ (X^T W_{0,2} + b_{1,2})^+ \end{bmatrix}^T W_{1,2} + b_{2,2} \right)^+$; that is, $v_{2,2}$ provides a further hyperplane refinement of \mathbb{R}^d .

To create a conceptual unification with forests, consider passing all the training data X through the network; for a network, the input X falls into a final network partition cell in the last internal layer

[26]. This partition cell is **encoded by the set of nodes** in the penultimate layer that are activated by **X** . This approach differs from forests: in a forest, the ensemble is realized by voting over a forest of trees, while in a network **each X can activate many (even all) cells in the penultimate layer, though with different activation energies**. In other words, both forests and networks can be seen to use the same representation space, though they achieve their particular representation via different estimation (“learning”) algorithms. Specifically, they both learn **piecewise linear activation functions** [28–31].

2.3 A Union of Convex Polytopes To provide a concrete illustrative example, consider the following experimental setup. We generated a two-dimensional Gaussian XOR dataset (Figure 3, left) as a benchmark with four spherically symmetric Gaussians. Class 0 has two Gaussians with centers $(-1, -1)$ and $(1, 1)$, whereas class 1 has two Gaussians with centers $(1, -1)$ and $(-1, 1)$. There are 5,096 random samples from the two classes, which are split into 4,096 training samples and 1,000 testing samples. We trained both forests and networks on such data. Figure 3 (center and right) shows the partitions learned by the two methods. More formally, let N_l be the set of nodes in a given layer l and let $A_l(x) = \{a \in N_l | a(x) > 0\}$, where a is the activation function of the underlying forests/networks. That is, A_l takes in an inference example as input and outputs the set of nodes *in a given layer* on which the input inference example activates. Now let $A_L = \bigoplus_{l=0}^L A_l$. Given an inference example as input, A_L outputs the concatenated set of nodes *in all layers up to and including layer L* on which the input inference example activates. In Figure 3 (center and right), similarly colored points output the same value of A_L . These collections of points are partitions, defined by $C_L(x) = \{z \in \mathcal{X} | A_L(z) = A_L(x)\}$ for a given inference point x , where \mathcal{X} is the domain of the forests/networks. In forests with L equal to the depth, this partition is a leaf cell. In networks with L equal to the total number of layers, this partition is a convex polytope.

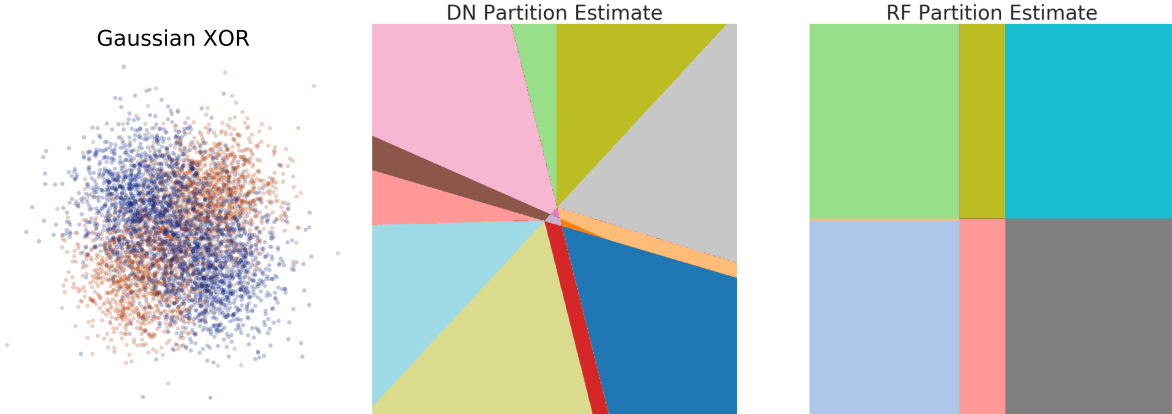


Figure 3: **(Left)** Gaussian XOR samples used as a benchmark. **(Center and right)** Visualizations of the partitions defined by C_L with respect to input space, \mathcal{X} , defined by a network **(center)** and a forest **(right)**. A unique region (i.e. part) is visualized by an arbitrary unique color and corresponds to a specific activation region. Note that the color value does not have any particular meaning.

In Figure 4, we visualize the layer-wise composition of C_L , the boundaries of C_l for all layers and for each node in each layer, and the effect of C_l on posteriors. This provides additional context for the creation of Figure 3.

3 Empirical Differences

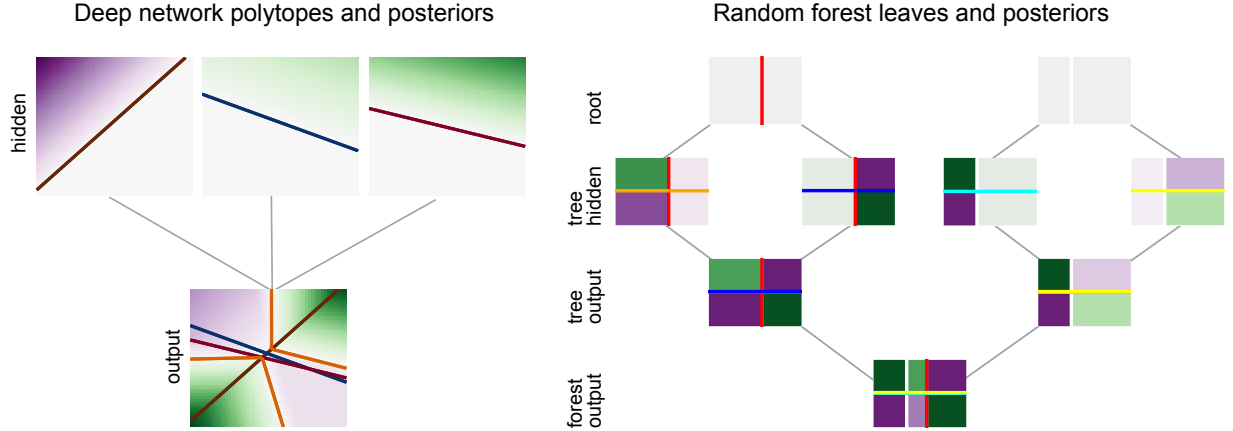


Figure 4: Visualizations of the polytope compositions for networks (**left**) and forests (**right**). For the first layer/depth polytopes/leaves, we show the boundary for which C_0 changes value. That is, on one side of the visualized boundary the node is activated; on the other side, the node is not activated. In the case of networks, this means that one side contains the linear portion of the ReLU activation, while the other side contains the 0-valued region of the ReLU activation; in the case of forests, this indicates to which subsequent node (either left or right) examples will recursively fall. For all polytopes/leaves in all subsequent layers/depths, we visualize the C_l boundaries for that layer, and we also overlay the boundaries of $C_{l'}$ for all previous layers $l' < l$. The bottom rows both indicate the final model cells C_L . In all nodes, the magnitude of the background color is determined by the activations of that layer, with class 0 being more purple, and class 1 being more green.

3.1 Tabular We used OpenML-CC18 for tabular benchmarks, which is a collection of 72 datasets organized by OpenML to function as a comprehensive benchmark suite [32, 33]. These datasets vary in sample size, feature space, and unique target classes. About half of the datasets are binary classification tasks, and the other half are classification tasks with up to 50 classes. The range of total sample sizes of the datasets is between 500 and 100,000, while the range of features is from a few to a few thousand. Datasets were imported using the OpenML python package, which is BSD-licensed [34].

3.1.1 Methods

Computing All datasets with over 10,000 samples were randomly downsampled to 10,000 samples. Then benchmarks were performed using 5-fold cross-validation, with the held-out test folds used to evaluate all classification tasks for the given dataset. Next, for each dataset’s training folds, the training data were indexed into eight subsets with evenly spaced sample sizes on a logarithmic scale, thus producing eight training sets with different sample sizes. The smallest of these sample sizes had five times the number of classes in the dataset, and the largest sample size used the entire training fold.

Random forest is a non-parametric and universally consistent estimator, so it will approach Bayes optimal performance with sufficiently large sample sizes, tree depths, and trees [35]. We used 500 trees with no depth limit, only varying the number of features selected per split (“max-features”). Letting d equal the number of features in the dataset, we varied max-features to be one of: \sqrt{d} , $d/4$, $d/3$, $d/1.5$, and d [36].

For optimizing hyperparameters in a network, we essentially followed the guidance of Bouthillier et al. [37]. MLPClassifier from the scikit-learn (BSD 3-Clause) package was used with one hidden layer [38]. The default setting was used for weight initialization, and the following parameters were

tuned: hidden layer size between 20 and 400, and the L2 regularization parameter along log-uniform from 1×10^{-5} to 1×10^{-2} . These parameters were determined based on previous classification work by Jurtz et al. [39] on the amino acid dataset [40]. To extend this optimization to over-parametrized networks, we also searched over the number of layers of the network from one to three hidden layers spanning all combinations of node sizes from 20 to 400.

For all hyperparameter tuning in both forests and networks, the tuning was conducted only on the entire dataset, using a randomized hyperparameter search with five folds. Tuned hyperparameters were then consistent for all smaller sample sizes per dataset. All tabular benchmarks were run on a 2.3 GHz 8-core Intel i9 CPU. Model training and hyperparameter tuning were parallelized using all available cores.

Evaluation Criteria Cohen’s Kappa ($\kappa = \frac{p_o - p_c}{1 - p_c}$, where p_o is the proportion of agreements, and p_c is the expected proportion of chance agreements) is an evaluation metric between two raters that determines the level of agreement between each [41]. To compare the performance of forests and networks, we subtracted networks’ Kappa from RF’s Kappa for each dataset at each sample size. Unlike classification accuracy, Cohen’s Kappa normalizes its score by accounting for chance accuracy. It can be a powerful tool for this experiment because, at small sample sizes, chance accuracy may have a large impact on the model evaluation. In the case of supervised classification, the two raters represent the predictions of the machine learning models and the ground truth of the data. The mean Kappa value was then recorded across the five folds for every sample size. A higher number represents higher accuracy, where a perfectly accurate model has a Kappa value of one.

Expected calibration error (ECE) is a metric used to compare two distributions by calculating the expected difference between accuracy and confidence [42]. In addition to Cohen’s Kappa, ECE was computed for each dataset, and comparison was calculated by subtracting networks’ ECE from RF’s ECE at each sample size. This method is executed by storing predictions in $N = 40$ equally spaced bins and calculating the weighted averages of the bins’ differences in accuracy versus confidence [43]. A lower number represents higher calibration, where a perfectly calibrated model has an ECE of zero.

Lastly, training wall times were recorded for both models. This metric calculated the fitting time for the given model after hyperparameter tuning, measured in seconds.

3.1.2 Results

Cohen’s Kappa and ECE Sample sizes are plotted on a logarithmic scale, whereas Cohen’s Kappa and ECE performance are plotted linearly (Figure 5). As seen from these results, there is a high level of variability between tabular datasets at each sample size. At larger sample sizes, forests tend to win Cohen’s Kappa and excel at accuracy, but networks would win ECE and achieve better calibration.

Training Wall Times Sample size have little impact on forest training wall times, yet there exists an overhead cost of slightly less than one second to fit these models (Figure 5). Networks, on the other hand, are an order of magnitude faster than forests at small sample sizes, but quickly increase to be an order of magnitude slower as sample size increase.

Given the OpenML-CC18 tabular dataset suite, there appears to be little relationship between average model performance and sample size. However, tabular benchmarks (Figure 5) show trends differentiating the classifiers’ ECE scores, which suggest that forests could produce better-calibrated models at small sample sizes. Should model calibration be the priority, this difference yields a framework for selecting the optimal method given the available sample size on general tabular data. The behavior of training wall times also suggests a trade-off for method choices. At larger sample sizes,

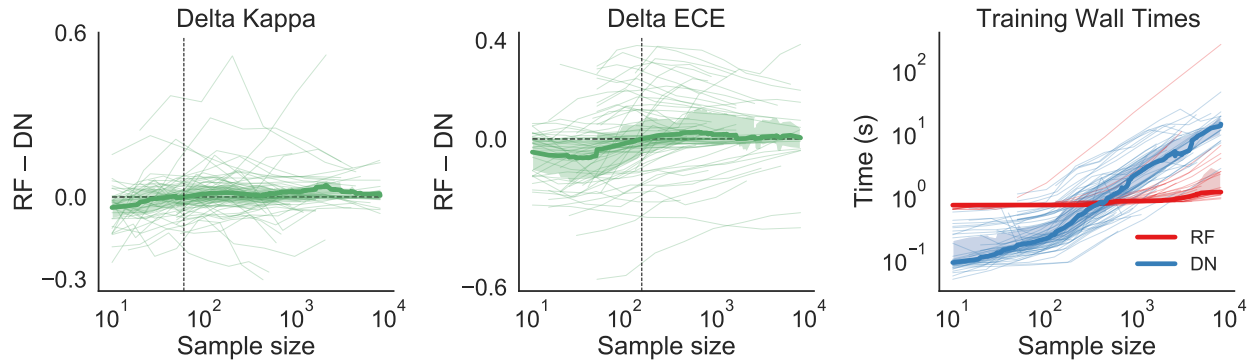


Figure 5: Performance of networks subtracted from performance of forests, evaluated using Cohen’s Kappa (**left**) and expected calibration error (ECE) (**center**); and training wall times of forests and networks (**right**). For all plots, thin lines represent individual datasets, and shaded regions highlight the 25th through 75th percentiles. Left plot illustrates delta Cohen’s Kappa versus sample size. Positive values mean better forest performance at the given sample size. Center plot illustrates delta ECE versus sample size. Negative values mean better calibration for forests. Thick green lines in both plots are the interpolated means over all datasets. Right plot shows training wall times versus sample size. Thick lines are the interpolated medians. Delta Kappa shows that forests are more accurate at larger sample sizes, while Delta ECE suggests that networks are better calibrated at larger sample sizes. For training wall times, networks are faster than forests at small sample sizes but slower at larger sample sizes.

network training times would scale much faster. If time is a limiting factor, then forests may be the ideal selection for novel tabular data at larger sample sizes.

3.2 Vision We used CIFAR-10 and CIFAR-100 datasets to evaluate the performance of forests and networks on vision data, primarily because of the number of classes and large sample sizes of these datasets [44]. Each dataset contains 60,000 colored images with 32x32 pixels, which are separated into 10 or 100 classes, resulting in 6,000 or 600 images per class. We also included the SVHN dataset as a supplement (Appendix B) [45]. Each high-dimensional image sample would be represented by RGB pixels and thus contain $32 \times 32 \times 3 = 3,072$ features.

3.2.1 Methods

Computing We experimented with multi-class classifications in 3-class, 8-class, and 90-class settings. We sampled the 3-class and 8-class training sets from the CIFAR-10 and SVHN datasets, and the 90-class training sets from the CIFAR-100 dataset. For each classification task, we ensured 45 random combinations of class labels and up to 10,000 training samples, stratifying data equally across the classes.

For classical architectures, we used `RandomForestClassifier` and `SVC` (“rbf” kernel) from the `scikit-learn` python package [38]. For the deep learning models, four convolutional neural network (CNN) architectures using ReLU activation were employed: three simpler models built with varying parameters and ResNet-18 [10, 16]. We adapted the pre-trained ResNet-18 classifier from PyTorch (BSD-3) as a robust choice and optimized its last layer with our training sets [46]. Among the three simpler CNNs, the first network is a simple architecture consisting of one convolutional layer of 32 filters with ReLU and one fully connected layer. The second CNN consists of two convolutional layers each with 32 filters and ReLU, followed by two fully connected layers with 100 and 10 nodes, respectively. Lastly, we constructed a CNN with five convolutional layers that scale up to 128 feature maps, and each layer is followed by batch normalization and ReLU. All convolutions end with one or two fully connected layers with ReLU.

For the high-dimensional vision data, our main principle of hyperparameter setup is to minimize tuning and benchmark models with their default values “out of the box” [47]. For RF and SVM-RBF, we used their default parameters of the scikit-learn library for all model aspects except RF’s number of concurrent jobs ran in parallel utilizing all the cores [38]. We benchmarked these models on two Microsoft Azure compute instances: a 2-core Standard_DS2_v2 (Intel Xeon E5-2673 v3) and a 6-core Standard_NC6 (Intel Xeon E5-2690 v3) (Table 1).

Compute Instance	vCPU	Memory: GiB	SSD: GiB	GPU	GPU Memory: GiB
Standard_DS2_v2	2	7	14	0	N/A
Standard_NC6	6	56	340	1	12

Table 1: Specifications for Azure compute instances.

We implemented all of our network models with a learning rate of 0.001 and a batch size of 64, using stochastic gradient descent with a momentum of 0.9 and cross-entropy loss. These hyperparameters were chosen either by default or commonly seen in literature, and for our training iterations, our settings provided the model with enough time to visually converge on the loss [6, 48]. We first implemented the networks with 30 epochs and activated early stopping when validation loss did not improve in three epochs in a row [49–51]. In these tasks, we randomly selected 30% of the provided test sets as validation data and only used the held-out 70% for benchmarks.

Alternative approaches restricted CNN epochs by calibrating their training wall times or money cost, conforming to those of RF as run on different compute instances. The alternative approaches used the full data of the provided test sets for benchmarks. All approaches were benchmarked on the 1-core GPU component of a Microsoft Azure compute instance: Standard_NC6 (NVIDIA Tesla K80). We utilized the GPU with the PyTorch CUDA library [46].

Evaluation Criteria We evaluated the performance by classification accuracy and training wall times. The training wall times calculated the fitting time for the given model after hyperparameter tuning, measured in seconds. The provided test sets were used.

3.2.2 Results

Unbounded Time and Cost The classification accuracy of RF and SVM-RBF are very similar, and SVM-RBF surpasses RF by a small margin at larger sample sizes (Figure 6). Both classifiers outperform the networks at smaller sample sizes. However, CNN accuracy often overcomes that of the classical models eventually. Higher class numbers decrease the accuracy of all models implemented, but the advantages of RF and SVM-RBF at smaller sample sizes also diminish as the number of classes increases. ResNet-18 with early stops completely surpasses both classical models in the 90-class classification task. Among the networks, more convolutional layers produce higher accuracy, and the performance of 5-layer CNN is very close to that of ResNet-18. ResNet-18 always surpasses other models at 10,000 samples.

Although RF and SVM-RBF have similar overall accuracy, SVM-RBF’s training wall times quadratically increase with the sample sizes and eventually surpass all other models’ (Figure 6). The training wall times of parallelized RF stay relatively constant until acquiring faster growths at larger sample sizes. With early stopping, CNNs would produce training time descents at around 100 samples and increase along with sample size again with slower growth rates. The training time trajectories of CNNs partially overlap each other and always stay higher than those of RF. Only the 90-class task produces noticeable differences for CNNs’ training wall times, which become more visible at larger sample sizes.

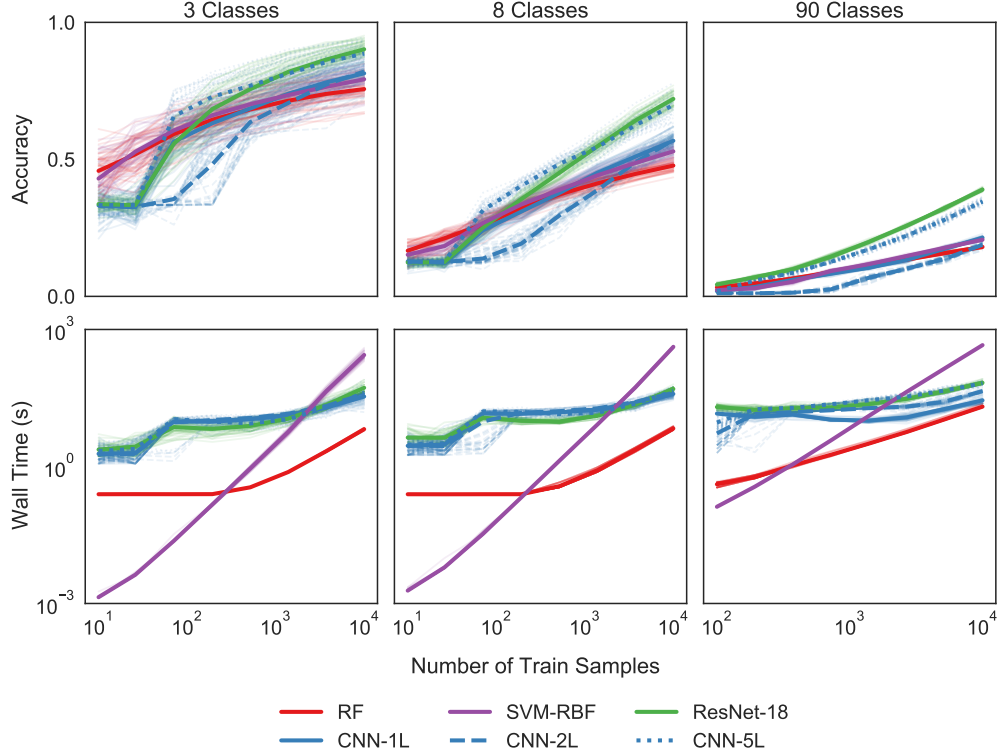


Figure 6: Performance of forests and networks on multiclass CIFAR-10/100 classifications with unbounded time and cost. Upper row shows classifier accuracy on a linear scale, and bottom row shows training wall times in seconds on a logarithmic scale. The x-axes correspond to logarithmic sample sizes for respective columns. Each panel shows average results over 45 random combinations. The left two columns use CIFAR-10, while the rightmost uses CIFAR-100. Compared to CNNs, RF and SVM-RBF perform better and faster at small sample sizes. While SVM-RBF’s training wall times increase quadratically, RF with similar performance is always more efficient than CNNs. As the class number increases, more complex networks have better classification accuracy and longer training wall times.

Fixed Training Time We then compared methods such that each took about the same time on the same virtual machine for 10,000 training samples. The baseline is RF’s training times when run on the 6-core Standard_NC6 Azure compute (Table 1). All training wall times except that of SVM-RBF reference conform to one shape (Figure 7). Under the resource constraints, all the accuracy trajectories of CNNs are lower than those in the unbounded benchmarks (Figure 6). Only at around 1,000 samples does CNN accuracy surpass that of RF, whereas 100 samples is the dividing point for benchmarks without restraints. ResNet-18 still has the highest accuracy at 10,000 samples, surpassing all other classifiers eventually. The results with fixed training cost are qualitatively similar (Figure 9).

Vision benchmarks with the CIFAR datasets show that networks would benefit from larger sample sizes and higher class numbers. More complex networks like ResNet-18 would achieve better performance (Figure 6). In contrast, RF and SVM-RBF maintain the advantage on classification accuracy at small sample sizes, especially when the training times are fixed (Figure 7).

3.3 Audition We performed benchmarks on the Free Spoken Digit Dataset (FSDD) (CC BY-SA 4.0) [52]. The dataset includes six different speakers pronouncing each of the 10 digits 50 times, for a total of 3,000 auditory recordings. Similar to the vision dataset analysis, we considered RF, SVM-RBF, and various CNN architectures with different layers.

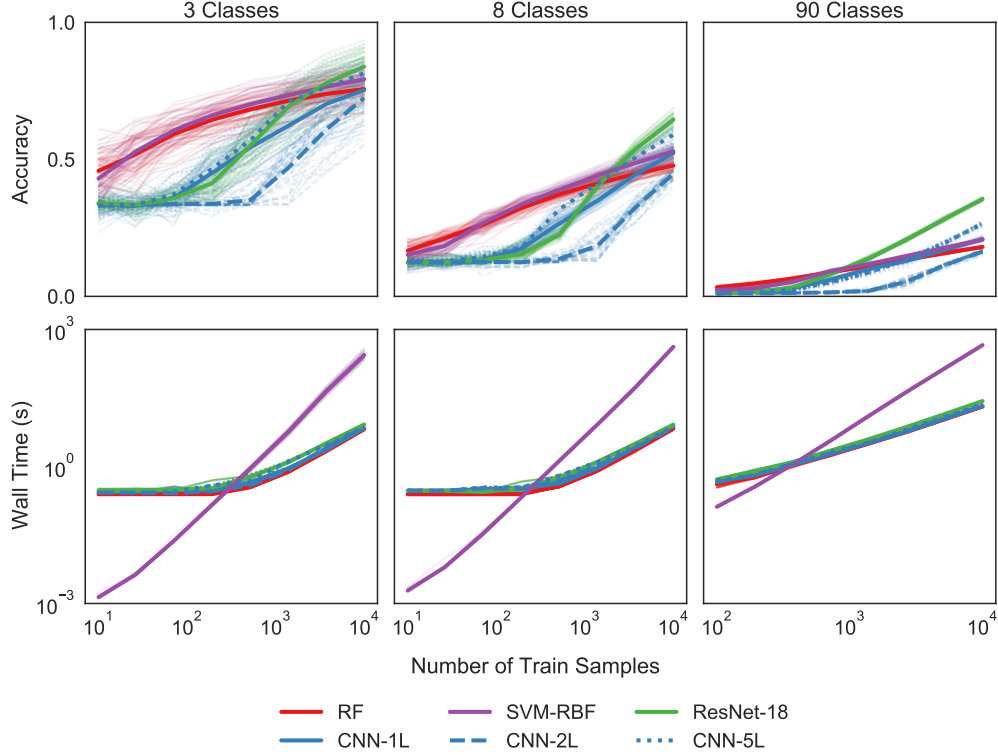


Figure 7: Performance of forests and networks on multiclass CIFAR-10/100 classifications with fixed training time. Upper row shows classifier accuracy on a linear scale, and bottom row shows training wall times in seconds on a logarithmic scale. The x-axes correspond to logarithmic sample sizes for respective columns. Each panel shows average results over 45 random combinations. The left two columns use CIFAR-10, while the rightmost uses CIFAR-100. RF and SVM-RBF have higher classification accuracy and lower training wall times compared to CNNs at smaller sample sizes. Complex networks, however, surpass RF and SVM-RBF at larger sample sizes, and ResNet-18 always performs best in the end.

3.3.1 Methods

Computing For the 3-class and 8-class training sets, we sampled 480 recordings by selecting 45 random combinations of class labels and stratifying data equally among the classes. We also randomly selected 10% of all the recordings for validation and another 10% for benchmarks [53, 54].

To preprocess the auditory files for networks, we used the short-time Fourier transform to convert the 8 kHz raw auditory signals into spectrograms [55]. In addition, we extracted mel-spectrograms (Appendix C) and mel-frequency cepstral coefficients (MFCCs) (Appendix D) using PyTorch’s inbuilt functions [46]. The size of fast Fourier transforms was set to 128 for spectrograms and mel-spectrograms, and 128 coefficients were retained for MFCC. We then scaled the data to zero mean and unit variance and reshaped the results into 32x32 single-channel images [56].

For RF and SVM-RBF, we still used `RandomForestClassifier` and `SVC` from the scikit-learn package [38]. Compared to the network architectures for vision data (Section 3.2), the only modification we made was setting the channel input to one for all the simpler CNNs. However, the pre-trained ResNet-18 requires three channels for RGB colors. To accommodate this requirement, we concatenated the images to two duplicates of themselves along the channel dimension. This new approach would be called ResNet-18-Audio for differentiation.

All hyperparameters were the same as those of vision analysis. We benchmarked the models on

the same Microsoft Azure compute with a 6-core CPU and a 1-core GPU: Standard_NC6 (Table 1).

Evaluation Criteria We evaluated the performance by classification accuracy. After training the classifiers, we benchmarked them using 10% of the dataset that was left aside, giving us 30 auditory samples per class. Thus, the test sets for the 3-class classification task have 90 auditory samples, while the 8-class test sets have 240 auditory samples.

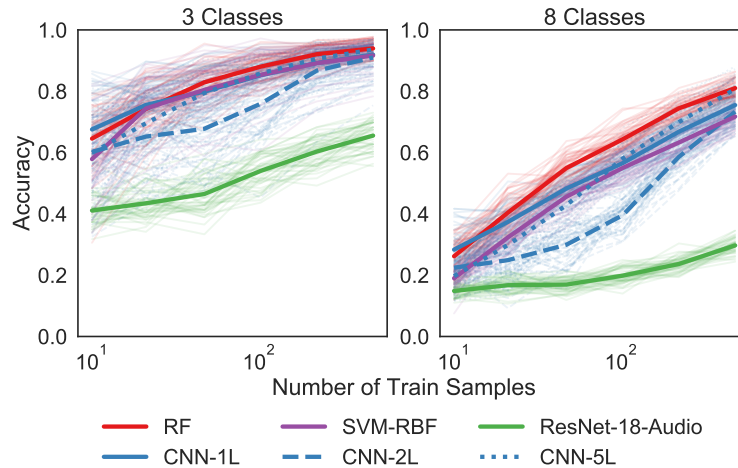


Figure 8: Performance of forests and networks on multiclass FSDD classifications using spectrograms. The y-axes represent classifier accuracy on a linear scale and the x-axes correspond to logarithmic sample sizes from 10 to 480. Each panel shows average results over 45 random class combinations and individual trajectories with lower alpha. In the 3-class task, RF, SVM-RBF, 1-layer, and 5-layer CNNs all have very similar performances. In the 8-class task, RF achieves the highest accuracy. ResNet-18-Audio performs much worse than other classifiers in both tasks.

3.3.2 Results

Spectrograms RF performs the best among all classifiers for essentially all sample sizes and all numbers of classes (Figure 8). ResNet-18-Audio has the worst performance in both tasks, presumably due to the small sample sizes that do not allow the complex network to train all its parameters effectively. The accuracy in the 8-class task compared to 3-class is lower for all models across all sample sizes. Thus, forests excel at auditory classifications at small sample sizes, while simpler networks would perform better than complex ones. The results with mel-spectrograms (Figure 11) and MFCCs (Figure 12) are qualitatively similar.

4 Discussion Conceptually, we described state-of-the-art machine learning methods simplified in classical statistical pattern recognition terms. The depiction of forests and networks as “partition and vote” schemes allows both a unified basic understanding of how these methods work from the perspective of classical classification and useful basic insight into their relationship with each other and potentially brain functions. Learning in biological brains can be viewed similarly as ensemble “partition and vote” functions implemented by a network of nodes. In brains, a “node” can correspond to a unit across many scales, ranging from synaptic channels (which can be selectively activated or deactivated due to the synapses’ local history), to cellular compartments, individual cells, or cellular ensembles [57]. At each scale, brains learn by partitioning feature space that is the set of all possible sensory inputs; a “part” corresponds to a subset of “nodes” that tend to respond to any given input. An example is the selective response properties that define cortical columns—columns in the sensory cortex [58]. Brains

also vote, where voting is a pattern of responses based on neural activation that indicate which stimulus evoked a response [59]. See Appendix E for further details.

Empirically, we provided comparisons for forests and networks on three data modalities and produced consistent results. Importantly, in the structured data scenarios, the input to networks typically includes not just the magnitude of each feature, but also the relative position of the features (for example, image pixels comprise a local patch as encoded into a convolutional layer). This is in contrast to forests, for which the input is purely the magnitude, without the relative location, of each feature. Thus, if each feature is encoded by a triple (m, x, y) , including the magnitude, horizontal, and vertical positions of the feature, forests tend to only get $1/3$ of the input that the networks get, significantly impoverishing the information they have to start with. In general, we found forests to excel at tabular and structured data (vision and audition) at small sample sizes, whereas networks performed better on structured data at larger sample sizes.

There do exist some limitations to this technical report, which we are planning to address in the coming months. Our next steps include: adding more metrics and stratifications to results, optimizing hyperparameter search for each sample size, and including other estimators in benchmarks, such as GBDT and sparse projection oblique randomer forests (SPORF) [23].

References

- [1] Jerome H. Friedman. Greedy function approximation: A gradient boosting machine. *The Annals of Statistics*, 29(5):1189–1232, 2001.
- [2] Rich Caruana and Alexandru Niculescu-Mizil. An empirical comparison of supervised learning algorithms. In *Proceedings of the 23rd International Conference on Machine Learning, ICML '06*, pages 161–168, New York, NY, USA, 2006. ACM.
- [3] Rich Caruana, Nikos Karampatziakis, and Ainur Yessenalina. An empirical evaluation of supervised learning in high dimensions. In *Proceedings of the 25th international conference on Machine learning*, pages 96–103, New York, New York, USA, July 2008. ACM.
- [4] Manuel Fernández-Delgado, Eva Cernadas, Senén Barro, and Dinani Amorim. Do we need hundreds of classifiers to solve real world classification problems? *Journal of Machine Learning Research*, 15(90):3133–3181, 2014.
- [5] Tianqi Chen and Carlos Guestrin. Xgboost: A scalable tree boosting system. In *Proceedings of the 22nd ACM SIGKDD International Conference on Knowledge Discovery and Data Mining, KDD '16*, pages 785–794, New York, NY, USA, August 2016. Association for Computing Machinery.
- [6] Alex Krizhevsky, Ilya Sutskever, and Geoffrey E Hinton. Imagenet classification with deep convolutional neural networks. In *Advances in Neural Information Processing Systems*, pages 1097–1105, 2012.
- [7] Yu Zhang, James Qin, Daniel S Park, Wei Han, Chung-Cheng Chiu, Ruoming Pang, Quoc V Le, and Yonghui Wu. Pushing the limits of semi-supervised learning for automatic speech recognition. arXiv preprint at <http://arxiv.org/abs/2010.10504>, October 2020.
- [8] Tom B Brown, Benjamin Mann, Nick Ryder, Melanie Subbiah, Jared Kaplan, Prafulla Dhariwal, Arvind Neelakantan, Pranav Shyam, Girish Sastry, Amanda Askell, Sandhini Agarwal, Ariel Herbert-Voss, Gretchen Krueger, Tom Henighan, Rewon Child, Aditya Ramesh, Daniel M Ziegler, Jeffrey Wu, Clemens Winter, Christopher Hesse, Mark Chen, Eric Sigler, Mateusz Litwin, Scott Gray, Benjamin Chess, Jack Clark, Christopher Berner, Sam McCandlish, Alec Radford, Ilya Sutskever, and Dario Amodei. Language models are few-shot learners. arXiv preprint at <http://arxiv.org/abs/2005.14165>, May 2020.
- [9] Nick Statt. Openai’s dota 2 ai steamrolls world champion e-sports team with back-to-back victories. <https://bit.ly/3o0ZLHs>, April 2019.
- [10] Kaiming He, Xiangyu Zhang, Shaoqing Ren, and Jian Sun. Deep residual learning for image recognition. arXiv preprint at <http://arxiv.org/abs/1512.03385>, 2015.
- [11] Ankit B. Patel, Tan Nguyen, and Richard G. Baraniuk. A probabilistic theory of deep learning. arXiv preprint at <http://arxiv.org/abs/1504.00641>, 2015.
- [12] Zhi-Hua Zhou and Ji Feng. Deep forest. *Natl Sci Rev*, 6(1):74–86, October 2018.
- [13] Wei Shen, Yilu Guo, Yan Wang, Kai Zhao, Bo Wang, and Alan Yuille. Deep differentiable random forests for age estimation. *IEEE Transactions on Pattern Analysis and Machine Intelligence*, 43(2):404–419, 2021.
- [14] Miguel A Carreira-Perpinan and Pooya Tavallali. Alternating optimization of decision trees, with application to learning sparse oblique trees. In S Bengio, H Wallach, H Larochelle, K Grauman, N Cesa-Bianchi, and R Garnett, editors, *Advances in Neural Information Processing Systems 31*, pages 1218–1228. Curran Associates, Inc., 2018.
- [15] Thomas M Hehn and Fred A Hamprecht. End-to-end learning of deterministic decision trees. In *Pattern Recognition*, pages 612–627. Springer International Publishing, 2019.
- [16] Carey E. Priebe, Joshua T. Vogelstein, Florian Engert, and Christopher M. White. Modern machine

- learning: Partition & vote. bioRxiv preprint at <https://www.biorxiv.org/content/10.1101/2020.04.29.068460>, September 2020.
- [17] Luc Devroye. On arbitrarily slow rates of global convergence in density estimation. *Zeitschrift für Wahrscheinlichkeitstheorie und Verwandte Gebiete*, 62:475–483, 1983.
 - [18] D.H. Wolpert and W.G. Macready. No free lunch theorems for optimization. *IEEE Transactions on Evolutionary Computation*, 1(1):67–82, 1997.
 - [19] C. Stone. Consistent nonparametric regression. *Annals of Statistics*, 5(2):595–645, 1977.
 - [20] L. Devroye, L. Györfi, and G. Lugosi. *A Probabilistic Theory of Pattern Recognition*. Springer, 1997.
 - [21] Leo Breiman. Random forests. *Machine Learning*, 45(1):5–32, 2001.
 - [22] Tyler M Tomita, Mauro Maggioni, and Joshua T Vogelstein. Roflmao: Robust oblique forests with linear matrix operations. In *Proceedings of the 2017 SIAM International Conference on Data Mining*, Proceedings, pages 498–506. Society for Industrial and Applied Mathematics, June 2017.
 - [23] Tyler M. Tomita, James Browne, Cencheng Shen, Jaewon Chung, Jesse L. Patsolic, Benjamin Falk, Carey E. Priebe, Jason Yim, Randal Burns, Mauro Maggioni, and Joshua T. Vogelstein. Sparse projection oblique randomer forests. *Journal of Machine Learning Research*, 21(104): 1–39, 2020.
 - [24] Yann LeCun, Yoshua Bengio, and Geoffrey Hinton. Deep learning. *Nature*, 521(7553):436–444, 2015.
 - [25] Vivienne Sze, Yu-Hsin Chen, Tien-Ju Yang, and Joel S Emer. Efficient processing of deep neural networks: A tutorial and survey. *Proceedings of the IEEE*, 105(12):2295–2329, 2017.
 - [26] Guido Montúfar, Razvan Pascanu, Kyunghyun Cho, and Yoshua Bengio. On the number of linear regions of deep neural networks. In *Proceedings of the International Conference on Neural Information Processing Systems*, pages 2924–2932, 2014.
 - [27] Guido Montúfar. Notes on the number of linear regions of deep neural networks. In *Sampling Theory and Applications*, Tallinn, Estonia, 2017.
 - [28] Thiago Serra, Christian Tjandraatmadja, and Srikumar Ramalingam. Bounding and counting linear regions of deep neural networks. In Jennifer Dy and Andreas Krause, editors, *IPAM*, volume 80 of *Proceedings of Machine Learning Research*, pages 4558–4566, Stockholmsmässan, Stockholm Sweden, 2018. PMLR.
 - [29] Yu Shi, Jian Li, and Zhize Li. Gradient boosting with piece-wise linear regression trees. arXiv preprint at <http://arxiv.org/abs/1802.05640>, 2019.
 - [30] David Rolnick and Konrad P Kording. Reverse-engineering deep relu networks. arXiv preprint at <https://arxiv.org/abs/1910.00744>, February 2020.
 - [31] Boris Hanin and David Rolnick. Complexity of linear regions in deep networks. In Kamalika Chaudhuri and Ruslan Salakhutdinov, editors, *Proceedings of the 36th International Conference on Machine Learning*, volume 97 of *Proceedings of Machine Learning Research*, pages 2596–2604. PMLR, 09–15 Jun 2019.
 - [32] Joaquin Vanschoren, Jan N. van Rijn, Bernd Bischl, and Luis Torgo. Openml: Networked science in machine learning. *SIGKDD Explorations*, 15(2):49–60, 2013.
 - [33] Bernd Bischl, Giuseppe Casalicchio, Matthias Feurer, Frank Hutter, Michel Lang, Rafael G. Mantovani, Jan N. van Rijn, and Joaquin Vanschoren. Openml benchmarking suites. arXiv preprint at <http://arxiv.org/abs/1708.03731>, 2019.
 - [34] Matthias Feurer, Jan N. van Rijn, Arlind Kadra, Pieter Gijsbers, Neeratyoy Mallik, Sahithya Ravi, Andreas Mueller, Joaquin Vanschoren, and Frank Hutter. Openml-python: an extensible python

- api for openml. arXiv preprint at <http://arxiv.org/abs/1911.02490>, 2019.
- [35] Gérard Biau, Luc Devroye, and Gábor Lugosi. Consistency of random forests and other averaging classifiers. *Journal of Machine Learning Research*, 9(66):2015–2033, 2008.
 - [36] Philipp Probst, Marvin N. Wright, and Anne-Laure Boulesteix. Hyperparameters and tuning strategies for random forest. *WIREs Data Mining and Knowledge Discovery*, 9(3):e1301, 2019.
 - [37] Xavier Bouthillier, Pierre Delaunay, Mirko Bronzi, Assya Trofimov, Brennan Nichyporuk, Justin Szeto, Naz Sepah, Edward Raff, Kanika Madan, Vikram Voleti, Samira Ebrahimi Kahou, Vincent Michalski, Dmitriy Serdyuk, Tal Arbel, Chris Pal, Gaël Varoquaux, and Pascal Vincent. Accounting for variance in machine learning benchmarks. arXiv preprint at <http://arxiv.org/abs/2103.03098>, 2021.
 - [38] F. Pedregosa, G. Varoquaux, A. Gramfort, V. Michel, B. Thirion, O. Grisel, M. Blondel, P. Prettenhofer, R. Weiss, V. Dubourg, J. Vanderplas, A. Passos, D. Cournapeau, M. Brucher, M. Perrot, and E. Duchesnay. Scikit-learn: Machine learning in Python. *Journal of Machine Learning Research*, 12:2825–2830, 2011.
 - [39] Vanessa Jurtz, Sinu Paul, Massimo Andreatta, Paolo Marcatili, Bjoern Peters, and Morten Nielsen. Netmhcpan-4.0: Improved peptide–mhc class i interaction predictions integrating eluted ligand and peptide binding affinity data. *The Journal of Immunology*, 199(9):3360–3368, 2017.
 - [40] Timothy J. O'Donnell, Alex Rubinsteyn, Maria Bonsack, Angelika B. Riemer, Uri Laserson, and Jeff Hammerbacher. Mhcflurry: Open-source class i mhc binding affinity prediction. *Cell Systems*, 7(1):129–132.e4, 2018.
 - [41] Jacob Cohen. A coefficient of agreement for nominal scales. *Educational and Psychological Measurement*, 20(1):37–46, 1960.
 - [42] Mahdi Pakdaman Naeini, Gregory Cooper, and Milos Hauskrecht. Obtaining well calibrated probabilities using bayesian binning. In *Twenty-Ninth AAAI Conference on Artificial Intelligence*, 2015.
 - [43] Chuan Guo, Geoff Pleiss, Yu Sun, and Kilian Q. Weinberger. On calibration of modern neural networks. In Doina Precup and Yee Whye Teh, editors, *Proceedings of the 34th International Conference on Machine Learning*, volume 70 of *Proceedings of Machine Learning Research*, pages 1321–1330. PMLR, 06–11 Aug 2017.
 - [44] Alex Krizhevsky. Learning multiple layers of features from tiny images. *University of Toronto*, 2012.
 - [45] Yuval Netzer, Tao Wang, Adam Coates, Alessandro Bissacco, Bo Wu, and Andrew Y. Ng. Reading digits in natural images with unsupervised feature learning. In *NIPS Workshop on Deep Learning and Unsupervised Feature Learning 2011*, 2011.
 - [46] Adam Paszke, Sam Gross, Francisco Massa, Adam Lerer, James Bradbury, Gregory Chanan, Trevor Killeen, Zeming Lin, Natalia Gimelshein, Luca Antiga, Alban Desmaison, Andreas Kopf, Edward Yang, Zachary DeVito, Martin Raison, Alykhan Tejani, Sasank Chilamkurthy, Benoit Steiner, Lu Fang, Junjie Bai, and Soumith Chintala. Pytorch: An imperative style, high-performance deep learning library. In H. Wallach, H. Larochelle, A. Beygelzimer, F. d'Alché-Buc, E. Fox, and R. Garnett, editors, *Advances in Neural Information Processing Systems 32*, pages 8024–8035. Curran Associates, Inc., 2019.
 - [47] Philipp Probst, Anne-Laure Boulesteix, and Bernd Bischl. Tunability: Importance of hyperparameters of machine learning algorithms. *Journal of Machine Learning Research*, 20(53):1–32, 2019.
 - [48] Leslie Rice, Eric Wong, and Zico Kolter. Overfitting in adversarially robust deep learning. In Hal Daumé III and Aarti Singh, editors, *Proceedings of the 37th International Conference on Machine Learning*, volume 119 of *Proceedings of Machine Learning Research*, pages 8093–8104. PMLR, 13–18 Jul 2020.

- [49] Mingchen Li, Mahdi Soltanolkotabi, and Samet Oymak. Gradient descent with early stopping is provably robust to label noise for overparameterized neural networks. In Silvia Chiappa and Roberto Calandra, editors, Proceedings of the Twenty Third International Conference on Artificial Intelligence and Statistics, volume 108 of Proceedings of Machine Learning Research, pages 4313–4324. PMLR, 26–28 Aug 2020.
- [50] Lutz Prechelt. Automatic early stopping using cross validation: quantifying the criteria. Neural Networks, 11(4):761–767, 1998.
- [51] Rich Caruana, Steve Lawrence, and C. Giles. Overfitting in neural nets: Backpropagation, conjugate gradient, and early stopping. In T. Leen, T. Dietterich, and V. Tresp, editors, Advances in Neural Information Processing Systems, volume 13. MIT Press, 2001.
- [52] Zohar Jackson, César Souza, Jason Flaks, Yuxin Pan, Hereman Nicolas, and Adhish Thite. Jakobovski/free-spoken-digit-dataset: v1.0.8, August 2018.
- [53] Seham Nasr, Muhannad Quwaider, and Rizwan Qureshi. Text-independent speaker recognition using deep neural networks. In 2021 International Conference on Information Technology (ICIT), pages 517–521, 2021.
- [54] Shuo Tian, Lianhua Qu, Lei Wang, Kai Hu, Nan Li, and Weixia Xu. A neural architecture search based framework for liquid state machine design. Neurocomputing, 443:174–182, 2021.
- [55] Lonce Wyse. Audio spectrogram representations for processing with convolutional neural networks. CoRR, abs/1706.09559, 2017.
- [56] Yann A LeCun, Léon Bottou, Genevieve B Orr, and Klaus-Robert Müller. Efficient backprop. In Neural networks: Tricks of the trade, pages 9–48. Springer, 2012.
- [57] Joshua T Vogelstein, Eric W Bridgeford, Benjamin D Pedigo, Jaewon Chung, Keith Levin, Brett Mensh, and Carey E Priebe. Connectal coding: discovering the structures linking cognitive phenotypes to individual histories. Current Opinion in Neurobiology, 55:199–212, 2019.
- [58] Vernon Mountcastle. The columnar organization of the neocortex. Brain, 120(4):701–722, 1997.
- [59] Christian K Machens, Ranulfo Romo, and Carlos D Brody. Flexible control of mutual inhibition: a neural model of two-interval discrimination. Science, 307(5712):1121–1124, 2005.
- [60] Eva A Naumann, James E Fitzgerald, Timothy W Dunn, Jason Rihel, Haim Sompolsky, and Florian Engert. From whole-brain data to functional circuit models: The zebrafish optomotor response. Cell, 167(4):947–960.e20, 2016.

Appendix A. CIFAR-10/100 Benchmarks with Fixed Training Cost. We also compared methods such that each took about the same cost on two virtual machines for 10,000 training samples (Figure 9). The baseline is RF’s training times as run on the 2-core Standard_DS2_v2 Azure compute instance (Table 1). The SVM-RBF benchmarks were also run on the same compute instance for reference. As a result, the training wall times of CNNs, which often use the minimum epoch number, are always lower than those of RF. Due to the CNNs’ different complexities, the correspondence between training costs becomes more accurate as the class number increases. The networks’ training time trajectories also overlap more completely. The results are qualitatively similar to CIFAR benchmarks with fixed training time (Figure 7).

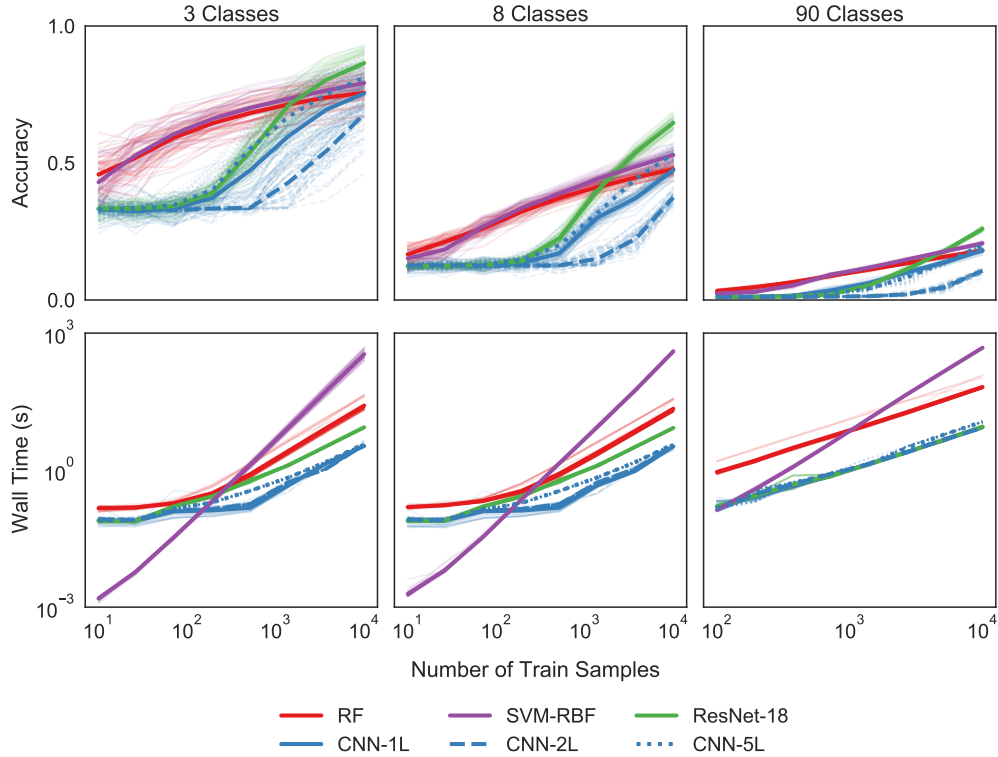


Figure 9: Performance of forests and networks on multiclass CIFAR-10/100 classifications with fixed training cost. Upper row shows classifier accuracy on a linear scale, and bottom row shows training wall times in seconds on a logarithmic scale. The x-axes correspond to logarithmic sample sizes for respective columns. Each panel shows average results over 45 random combinations. The left two columns use CIFAR-10, while the rightmost uses CIFAR-100. RF and SVM-RBF have higher classification accuracy and lower training wall times compared to CNNs at smaller sample sizes. Complex networks, however, surpass RF and SVM-RBF at larger sample sizes, and ResNet-18 always performs best in the end.

Appendix B. SVHN Benchmarks. The SVHN dataset contains 73,257 digits for training and 26,032 for testing [45]. The 3-class and 8-class tasks show surprising trends for networks, as simpler CNNs surpass ResNet-18 on classification accuracy as sample size increases. At higher sample sizes, 5-layer CNN has the best performance among all classifiers. Network accuracy is always higher than that of RF and SVM-RBF at 10,000 samples (Figure 10). Although RF and SVM-RBF perform better than networks at smaller sample sizes in the 3-class task, the advantages disappear in the 8-class task. As seen in the CIFAR benchmarks (Figure 6, 7, 9), networks would be more adept at handling higher class numbers.

The trends of training wall times are very similar to those of CIFAR benchmarks with unbounded time and cost (Figure 6). Forests’ training times are always shorter than networks’, and more fluctuations occur for CNN trajectories.

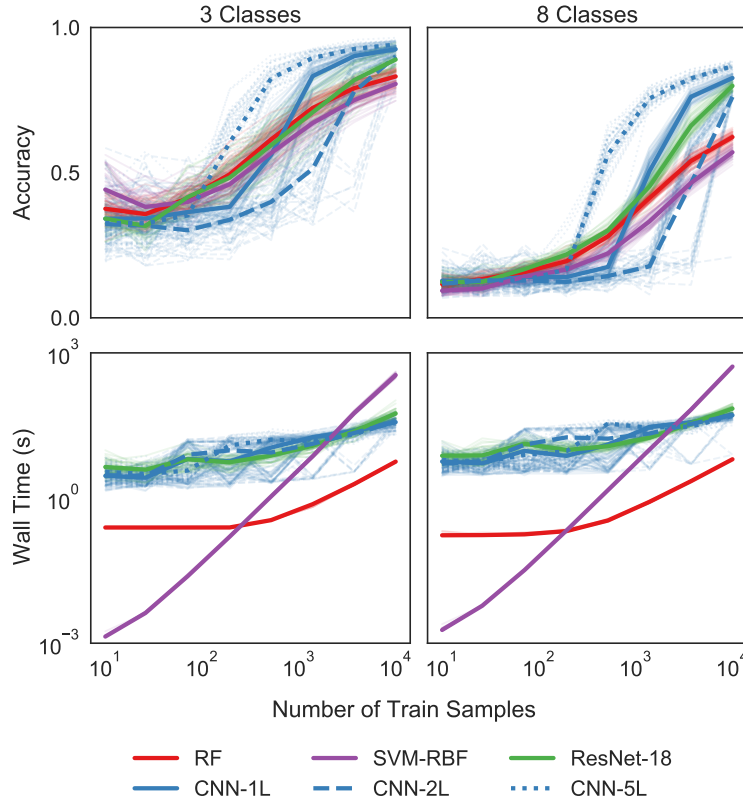


Figure 10: Performance of forests and networks on multiclass SVHN classifications with unbounded time and cost. Upper row shows classifier accuracy on a linear scale, and bottom row shows training wall times in seconds on a logarithmic scale. The x-axes correspond to logarithmic sample sizes for respective columns. Each column shows average results over 45 random combinations. Compared to CNNs, RF and SVM-RBF perform better and faster at smaller sample sizes.

Appendix C. FSDD Benchmarks with Mel-Spectrograms. As an alternative approach, we used PyTorch’s inbuilt function and converted the raw audio magnitudes into mel-spectrograms [46]. The process involves the aforementioned spectrogram conversions and uses triangular filterbanks to modify the images. The results (Figure 11) are qualitatively similar to FSDD benchmarks with spectrograms (Figure 8) and MFCCs (Figure 12).

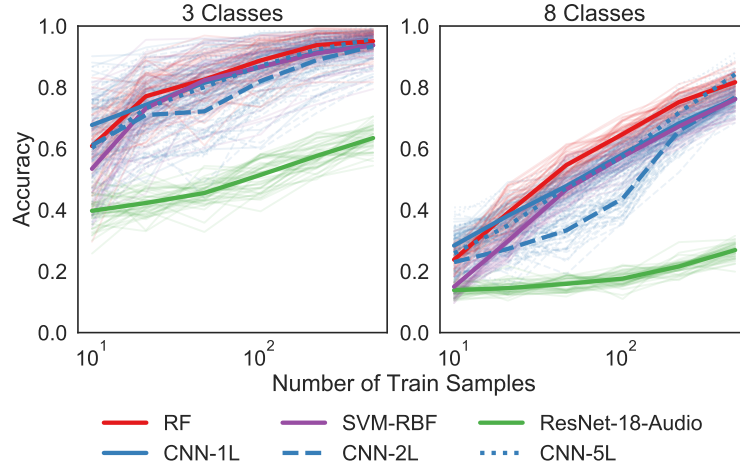


Figure 11: Performance of forests and networks on multiclass FSDD classifications using mel-spectrograms. The y-axes represent classifier accuracy on a linear scale and the x-axes correspond to logarithmic sample sizes from 10 to 480. Each panel shows average results over 45 random class combinations and individual trajectories with lower alpha. In the 3-class task, RF, SVM, 1-layer, and 5-layer CNNs all have very similar performances. In the 8-class task, RF achieves the highest accuracy. ResNet-18-Audio performs much worse than other classifiers.

Appendix D. FSDD Benchmarks with MFCCs. As an alternative conversion, we used PyTorch’s inbuilt function and converted the raw audio magnitudes into MFCC [46]. The process calculates MFCCs on the DB-scaled mel-spectrograms. The results (Figure 12) are qualitatively similar to FSDD benchmarks with spectrograms (Figure 8) and mel-spectrograms (Figure 11).

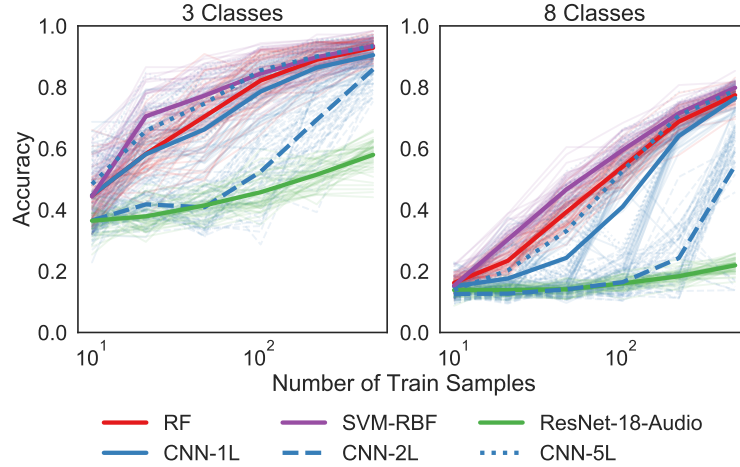


Figure 12: Performance of forests and networks on multiclass FSDD classifications using mel-frequency cepstral coefficients (MFCC). The y-axes represent classifier accuracy on a linear scale and the x-axes correspond to logarithmic sample sizes from 10 to 480. Each panel shows average results over 45 random class combinations and individual trajectories with lower alpha. SVM-RBF achieved the best performance in both tasks, but the advantage diminishes as the sample size increases. At the maximum sample size, RF, SVM, 1-layer, and 5-layer CNNs all have very similar accuracy. 2-layer CNN performs worse, while ResNet-18-Audio performs the worst.

Appendix E. Zebrafish Brain Maps. Figure 13 illustrates neural selectivity to features of sensory input in a larval zebrafish, and indicates a learned partition and vote framework for brain functioning [60]. Specifically, this image shows all motion-sensitive nodes ($n = 76,604$) in a brain. Each node is a dot, color coded for preferred motion direction. The image indicates that each node's activity indeed corresponds to a partition of feature space, which is actively refined through sensory experience and learning. A relationship with forests and networks, at least at a basic level, is clear. The utility of this relationship, for either machine learning or neuroscience, is the subject of endless conjecture and refutation.

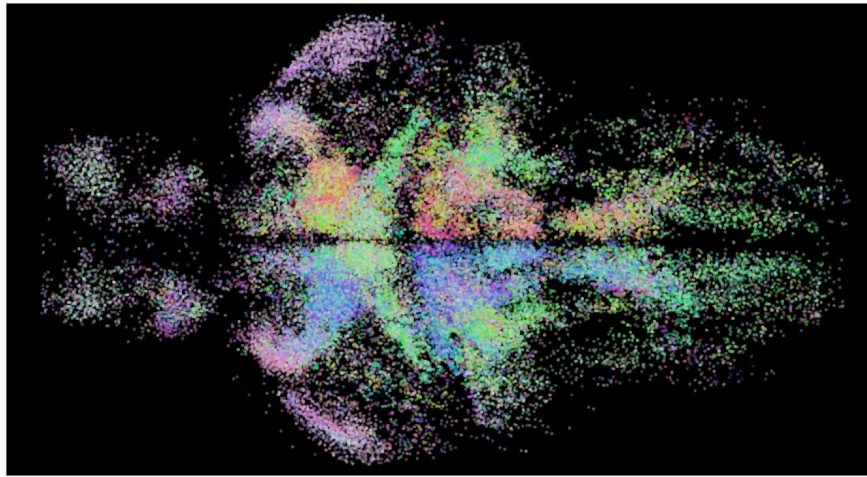


Figure 13: Whole-brain activity maps reveal processing stages underlying the optomotor response in a larval zebrafish.